Hindawi
Journal of Nanomaterials
Volume 2022, Article ID 3406405, 12 pages
https://doi.org/10.1155/2022/3406405

Research Article

Fluorination of Defective Titanium Dioxide with an Efficient Photocatalytic Activity

Yijie Zhao,[1] Xuan Hu,[1] Rongrong Hu,[1] Xingjian Wang,[1] Zhangyu Gu,[1] Xiaojuan Zhang,[1] and Yuan Zhao [1,2]

[1]*School of Materials Engineering, Jinling Institute of Technology, Nanjing 211169, China*
[2]*School of Energy and Power Engineering, Nanjing University of Science and Technology, Nanjing 210094, China*

Correspondence should be addressed to Yuan Zhao; yuanzhao@jit.edu.cn

Received 22 August 2022; Revised 23 September 2022; Accepted 10 October 2022; Published 26 December 2022

Academic Editor: Ganesan Sriram

Fluorinated-defective titanium dioxide (F-TiO_{2-x}) was successfully synthesized by fluorination of TiO_2 through the hydrothermal method. The microstructure and physicochemical properties of the catalyst were characterized by scanning electron microscopy, transmission electron microscopy, X-ray diffraction, X-ray photoelectron spectroscopy, and UV–vis diffuse reflectance spectroscopy (UV–vis DRS). As expected, F-TiO_{2-x} demonstrates high photocatalytic activity and stability on dye degradation. Results indicated that fluorine element can effective for stabilizing Ti^{3+} and oxygen vacancies on the surface of F-TiO_{2-x}. With the increase in the amount of hydrofluoric acid (HF) added, the photocatalytic performance of the prepared material is first increased and then decreased, and the catalyst shows the best performance when the amount of HF added is 0.3 mL. For three different dyes, the catalysts all showed a certain photocatalytic degradation performance, and the degradation effect of rhodamine B was the best.

1. Introduction

With the development of human society, energy crisis, and environmental pollution have become the serious topics in the scientific community. Organic pollutants in water seriously endanger human health [1]. Therefore, more attempts have been implemented to eliminate or reduce harmful compounds that are important for economic and social developments [2, 3]. As a standard technique, semiconductor-based photocatalysis is a predictable approach to play an imperative role in solving this problem [4–10]. Particularly, TiO_2 is attracting much attention due to its superior abilities, such as nontoxic, environmentally friendly, and low cost [11–13]. However, only a narrow range of the solar spectrum can be absorbed by TiO_2, most of which is ultraviolet, due to its large bandgap (~3.2 eV for anatase). Overcoming electron–hole pairs through unbalanced photogenerated recombination on the surface of crystallites has become an important prerequisite for the commercial application of TiO_2 [14, 15].

Special facet exposure on TiO_2 samples is an effective way to improve the separation of photogenerated electrons and holes, electrons are enriched in the (101) plane, whereas holes are enriched in the (001) plane, which ultimately contributes to the photocatalysis [16–18]. For TiO_2, the exposed crystal plane is generally the (101) crystal plane, the crystal plane energy (0.44 J/cm^2) of this crystal plane is low, and it has good reducing ability; therefore, it has good performance in photocatalytic hydrogen production, but its activity in degrading pollutants is lower than (001) [19]. Preliminary research shows that Ti^{3+} self-doped TiO_{2-x} prepared by the reduction method has good photocatalytic degradation performance [20, 21]. However, the instability of surface Ti^{3+} seriously hinders the photocatalytic performance of the catalyst. At the same time, different crystal planes of the photocatalytic materials tend to have different surface energies, and the crystal planes with high crystal plane energy tend to have higher oxidizing ability which is beneficial for the degradation of pollutants [22].

Currently, the methods of exposing crystal planes mainly include chemical etching and high-pressure treatment [23]. Under these circumstances, in order to obtain surfaces with higher reactivity, developing TiO_2 crystals with specific facets

has recently been investigated as an effective method to improve their efficiency [24, 25]. Numerous studies have shown that the surface fluorination treatment can stabilize the surface Ti^{3+} and oxygen vacancies, and expose special crystal planes [26, 27]. Zhang et al. found a significant enhancement on photocatalytic activity of TiO_2 powders by doping with F^- ions, and F ions not only suppressed the formation of brookite phase but also prevented phase transition of anatase to rutile [28]. Choi's research shows that the formation of surface fluorides on TiO_2 (F-TiO_2), which can be easily attained by a simple addition of F^- to aqueous TiO_2 suspensions, uniquely affects both photocatalytic reactions and photoelectrochemical behaviors [29]. Leung et al. studied the effect of F ion content in F-doped TiO_2 nanosheets on the photocatalytic degradation of toluene in vacuum ultraviolet. The results show that F ion-doped TiO_2 can enhance the photocatalytic activity mainly due to the improvement of the light absorption and the reduction of recombination efficiency of photogenerated carriers [30]. Despite the above-mentioned progress so far, F-doped TiO_2 photocatalytic materials have not been deeply studied as a promising photocatalytic hybrid material. In particular, the photocatalytic efficiency of F-titania is far from practical application.

Methyl orange (MO) is the most commonly used acid–base indicator and has good pH sensitivity. Under acidic and alkaline conditions, azo and quinoid structures are the main structures of dye compounds and are often chosen as dye models. Methylene blue (MB) is a common dye in the printing and dyeing industry. It is difficult to be oxidized in the environment and its degradation and decolorization is also an important object in the treatment of wastewater. In addition, MB is often used as a simulated pollutant. It is widely used in experimental research. Rhodamine B (RhB) is also a widely used heterocyclic dye. The wastewater of RhB has the characteristics of high chroma, high concentration, poor biodegradability, and difficult biochemical treatment. The photodegradation comparison of the above three organic dyes is of great significance for the study of the application of photocatalysts.

Herein, F-TiO_{2-x} were prepared by fluorination of TiO_2 through hydrothermal method. The degradation performance of d rhodamine B for F-TiO_{2-x} is much higher than TiO_{2-x}. The enhanced photocatalytic activity is attributed to the high-energy crystal face (001) and stabilized surface Ti^{3+}, which significantly reduces the recombination rate of photogenerated electrons and holes. The degradation rate of MO and MB for F-TiO_{2-x} is improved, which indicates that it has good applicability.

2. Experimental Section

2.1. Materials. Tetrabutyl titanate (TBOT), hydrochloric acid (HCl), hydrofluoric acid (HF), and ethanol were provided by NanJing chemical Reagent Co., Ltd., China. RhB, MO, MB, and barium sulfate were purchased from Aladdin Industrial Corporation. Sodium hydroxide and hydrazine hydrate were purchased from Sinopharm Chemical Reagent Co., Ltd., China. The deionized water used was produced in lab. All chemical reagents used in this experiment were of analytical grade, procured commercially, and used without further purification.

2.2. Preparation of Surface Fluorinated TiO_{2-x}. 3 mL TBOT was added into 30 mL HCl solution (0.1 mol/L), stir with a magnetic stirrer, and then 0.6 mL hydrazine hydrate was added during the stirring process. Continue stirring at room temperature for 30 min to obtain a yellow–brown precursor mixed solution, then a certain amount (0, 0.15, 0.3, 0.6, and 0.9 mL) of HF was added to the mixture. Transfer the mixed solution to 50 mL of teflon autoclave and heated at 180°C for 24 hr in an oven. After cooling to room temperature, the samples were washed three times with water and alcohol, respectively, and then dried in vacuum oven at 60°C for 6 hr. The samples were named TiO_{2-x}–n (n is the amount of HF used).

2.3. Characterization. The prepared samples were measured by X-ray diffraction (XRD) patterns (Bruker D8 Advance diffractometer) at room temperature with Cu Kα radiation ($\lambda = 0.15418$ nm). X-ray photoelectron spectra (XPS) of samples were collected using PHI 5000 VersaProbe II. UV–vis diffuse reflectance spectroscopy (DRS) was obtained on a UV-1800 UV–vis spectrophotometer. The surface morphology of composite catalysts was analyzed by scanning electron microscopy (SEM) using Hitachi S-4800 scanning electron microscope, and the accelerating voltage is 10 kV. Transmission electron microscopy (TEM) micrographs were obtained by JEOL JEM-2100F microscope (Japan) that was operated at an accelerating voltage 200 kV. Brunner−Emmet−Teller (BET) surface area measurements were carried out by N_2 adsorption at 77 K using an ASAP2020 instrument.

2.4. Photocatalytic Experiment. The photocatalytic performance of samples was evaluated by photodegradation of dyes under 300 W xenon lamp with a UV cut-off filter ($\lambda > 420$ nm). The photocatalytic experiments were carried out as follows: 50 mg of photocatalyst were dispersed in the breaker containing 50 mL of 10 mg/l dye aqueous solution under continuously stirring at room temperature. After stirring the solution in dark for 30 min to achieve the adsorption–desorption equilibrium, the xenon lamp was turned-on and 5 mL of suspension was taken out in every 5 min. The suspension was immediately centrifuged to obtain supernatant at 8,000 rpm for 5 min. The absorbance of the supernatant was measured at 554 nm through UV–visible spectrophotometer. The photocatalytic performance is evaluated in two ways. One is the degradation efficiency of dye by photocatalyst. The other is to indirectly reflect the degradation rate of the catalyst according to the reaction kinetic constant of photocatalysis.

3. Results and Discussion

Figure 1(a) shows the comparison of the photocatalytic degradation performance of RhB by catalysts prepared with different amounts of HF. The photocatalytic degradation performance does not show a linear relationship with the amount of HF used. When the amount of HF used was 0.3 mL, the prepared photocatalyst had the best

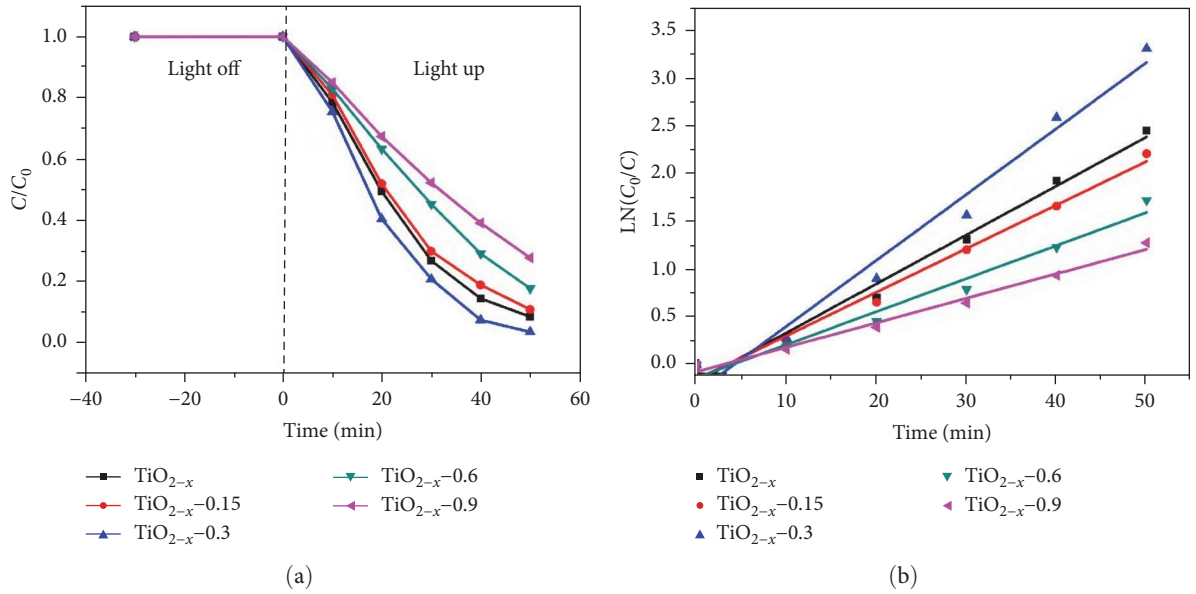

Figure 1: (a) Degradation performance diagram of F-TiO_{2-x} catalyst prepared with different HF usage; (b) quasi-first-order kinetic fitting.

Table 1: Pseudo-first-order kinetic constants of rhodamine B degradation by F-TiO_{2-x} prepared with different amounts of HF.

Sample	TiO_{2-x}	TiO_{2-x}–0.15	TiO_{2-x}–0.3	TiO_{2-x}–0.6	TiO_{2-x}–0.9
Kinetic constant (min^{-1})	0.051	0.045	0.068	0.035	0.025

photocatalytic degradation performance of RhB, the degradation rate of RhB reached 96.8% in 50 min of illumination. Figure 1(b) is the first-order kinetic constant curve calculated according to the fitting; it can be seen that with the increased amount of HF used, the reaction rate first decreases, then increases and then decreases; the specific kinetic constants are shown in Table 1; the first-order kinetic constant K_{app} first decreased, then increased and then decreased. The reason for this may be that with the increase of HF, the high-energy (001) crystal face is exposed on the one hand, which increases the surface activity of the catalyst. On the other hand, with the increase in the amount of HF, HF inhibits the crystal transformation, promotes the grain growth of the material, reduces the specific surface area, and then reduces the active center of the reaction, the photocatalytic degradation efficiency is reduced. The degradation rate of TiO_{2-x}–0.3 was 27% higher than that of TiO_{2-x}.

In order to obtain the substance type and grain size of F-TiO_{2-x} prepared by different fluorination treatments, XRD analysis was performed on the prepared materials, and the analysis results are shown in Figure 2. The XRD patterns of TiO_{2-x}, TiO_{2-x}–0.15, TiO_{2-x}–0.3, TiO_{2-x}–0.6, and TiO_{2-x}–0.9 show the obvious peaks at 25.3°, 36.9°, 37.8°, 38.6°, 48.1°, 53.9°, 55.1°, 62.1°, 62.7°, and 68.8° are correspond to the crystal plane peaks of (101), (103), (004), (112), (200), (105), (211), (213), and (204) of anatase type TiO_2 (PDF No. 99-0008) [31, 32]. TiO_{2-x} without fluorination showed obvious peaks at 27.4°, 36.1°, and 56.6° corresponding to the (110), (101), and (220) crystal planes of rutile TiO_2, respectively, according to the PDF No. 99-0090 standard card [33, 34]. The analysis results show that fluorine atoms inhibit the anatase–rutile transition. In addition, with the increase of the degree of fluorination, the sharpness of the characteristic peak of the (101) crystal plane at 25.3° increased continuously, indicating that the fluorination treatment improved the crystallinity of the material. Table 2 shows that the grain size and phase ratio of the material were calculated according to the Scherrer formula and the empirical formulas. According to the calculation results in Table 2, it can be seen that the presence of fluorine promotes the grain growth.

XPS was used to analyze and test the elemental composition and valence state of the TiO_{2-x}–0.3 surface. Figure 3 shows the full spectrum of TiO_{2-x}–0.3 and the high-resolution XPS images of C1s, N1s, O1s, F1s, and Ti2p. The results of the fit to the test data are also shown in Figure 3. Figure 3(a) shows the full spectrum of TiO_{2-x}–0.3; it can be seen from the figure that there are elements such as C, N, O, F, and Ti on the surface of the material, indicating that F was successfully introduced into the surface of TiO_2. Figure 3(b) is the high-resolution XPS image of C1s, which only has a peak at 284.8 eV, which is caused by the surface adventitious carbon. Figure 3(c) is the high-resolution XPS image of N1s. Through fitting analysis, there are binding energy peaks at 401 and 399.5 eV. The former is because N replaces O to form O–Ti–N, and the latter is because N atoms enter lattice gap. Figure 3(d) is the high-resolution XPS image of O1s. It is obtained by fitting that the binding energy peaks appear at 529.5 and 531.6 eV, which are due to the existence of lattice oxygen and surface

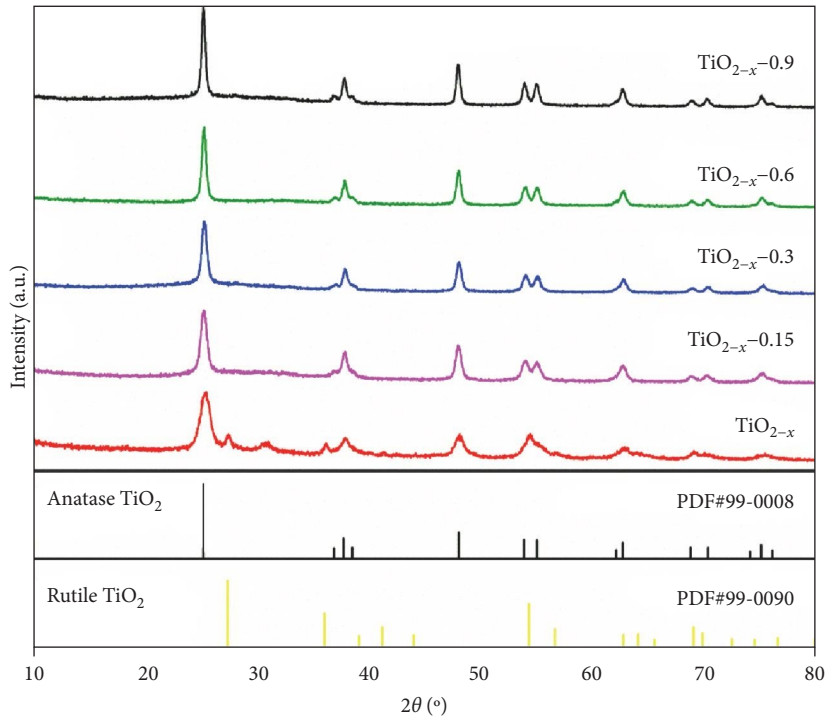

Figure 2: XRD patterns of F-TiO_{2-x} catalysts prepared with different amounts of HF.

Table 2: Crystal forms and grain sizes of F-TiO_{2-x} prepared with different amounts of HF.

Sample	Crystal ratio (%)		Grain size (nm)
	Anatase	Rutile	
TiO_{2-x}	81	19	20
TiO_{2-x}–0.15	100	0	26
TiO_{2-x}–0.3	100	0	31
TiO_{2-x}–0.6	100	0	46
TiO_{2-x}–0.9	100	0	122

hydroxyl and adsorbed oxygen, respectively [35]. Figure 3(e) shows that the central peak of F1s located at 684.3 eV, which is a typical characteristic peak of fluorinated TiO_2, and F plays a pivotal role in the formation of Ti^{3+} or oxygen vacancies [36, 37]. Figure 3(f) is the high-resolution XPS image of Ti2p, the peaks are located at binding energies 464.3, 458.5, 463.5, and 458.0 eV, corresponding to Ti^{4+} $2p_{1/2}$, Ti^{4+} $2p_{3/2}$, Ti^{3+} $2p_{1/2}$, and Ti^{3+} $2p_{3/2}$, respectively. The fitting results show that Ti^{3+} exists on the surface of TiO_{2-x}–0.3 [38].

Figure 4(a) shows the morphological characteristics of the sample TiO_{2-x} without fluorination treatment. It can be seen from the figure that the particles are relatively uniform and block-like, and the particle size is about 20 nm. Figure 4(b) is the topography image of the sample TiO_{2-x}–0.15. It can be seen from the figure that compared with TiO_{2-x}, the sharp edges of TiO_{2-x}–0.15 are gradually etched, and the particle shapes are diversified and growing trend. As shown in Figures 4(c) and 4(d), the HF usage continues to increase, the TiO_2 particles are continuously etched, and these particles are self-assembled to form large particles. As shown in Figure 4(d) that when the amount of HF used is 0.6 mL, large particles with a particle size larger than 200 nm have been formed. Figures 4(e) and 4(f) are the TEM and SEM images of the sample TiO_{2-x}–0.9, respectively. From the TEM and SEM morphology images, it can be found that the small bulk particles have disappeared, and the grains are all larger than 100 nm. With the addition of HF, the edges of the TiO_2 particles were gradually etched, and these particles are self-assembled eventually to form large particles [30].

Figure 5 is the TEM image, particle size distribution image, and high-resolution transmission electron microscope (HRTEM) image of TiO_{2-x}–0.3. Figure 5(a) shows that the particles have good dispersion and are mainly polygonal. The particle size distribution statistics are carried out, and the statistical results are shown in Figure 5(b). It can be seen from the figure that the particle size distribution is between 20 and 60 nm, and the average particle size is 35 nm, which is basically consistent with the XRD analysis and calculation results. Figure 5(c) is the HRTEM image of TiO_{2-x}–0.3, and Figure 5(d) is its partial enlarged image. The lattice fringe spacings are 0.352 and 0.237 nm, respectively, and the angle between the crystal planes is 68.3°, which exactly matches the theoretical value of the angle between the (101) and (001) crystal planes [39, 40]. Studies have shown that holes tend to migrate to the high-energy (001) crystal plane, whereas electrons tend to aggregate at the (101) crystal plane, thereby separating electrons and holes [41, 42].

It was observed that the particle size of TiO_2 gradually increased with the increase of HF usage in the SEM and TEM images. In general, the increase in particle size of nanomaterials leads to a decrease in specific surface area. To further

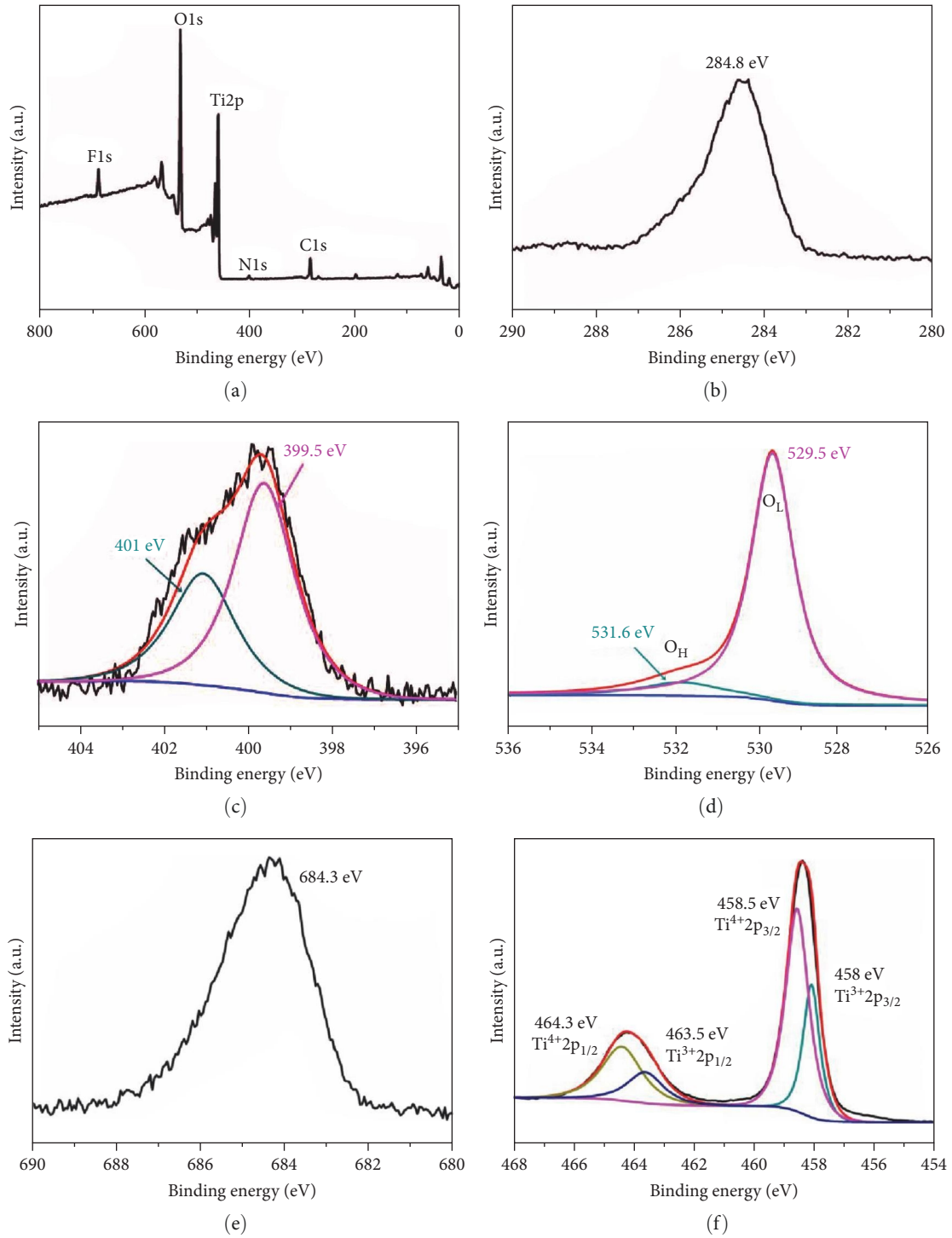

FIGURE 3: (a) Full spectrum of TiO_{2-x}–0.3; (b) C1s; (c) N1s; (d) O1s; (e) F1s; (f) Ti2p high-resolution XPS image.

confirm the effect of HF usage on the specific surface area of TiO_2, BET tests were performed on the samples. Figure 6 is the nitrogen adsorption/desorption isotherms of samples prepared with different HF usages, and Table 3 shows the specific surface area values of the samples. The specific surface area of the sample TiO_{2-x} without fluorination treatment reached 81 m^2/g. After the fluorination treatment, the specific surface area of the sample decreased, and with the increase in HF usage, the specific surface area of the sample continued to decrease. The specific surface area of the sample TiO_{2-x}–0.9 is only 28.5 m^2/g, which is only one-third of TiO_{2-x} without fluorination treatment. The result was consistent with the SEM and TEM.

In order to understand the effect of fluorination treatment on the light absorption properties of the materials and to analyze and calculate the bandgap width of the materials,

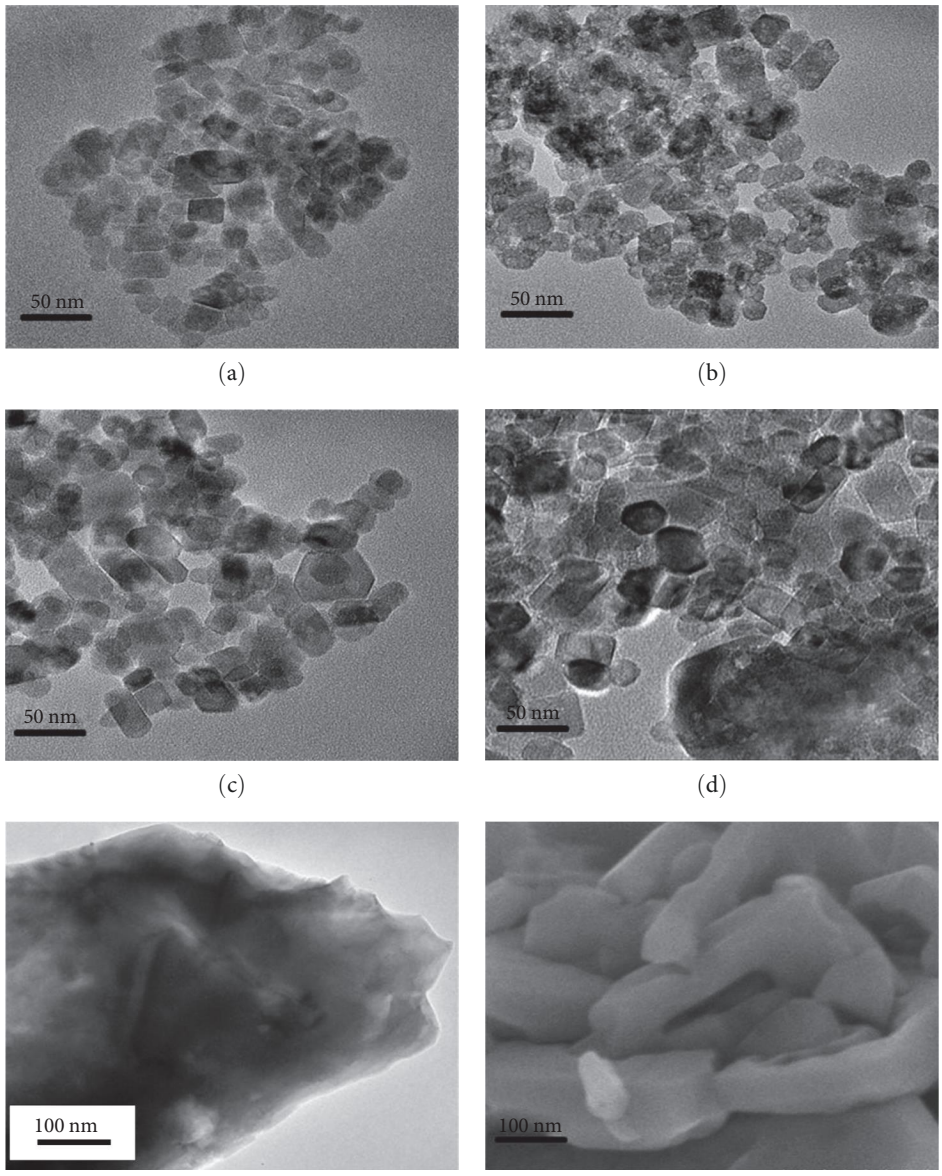

FIGURE 4: TEM images of F-TiO_{2-x} prepared with different HF usage: (a) TiO_{2-x}; (b) TiO_{2-x}–0.15; (c) TiO_{2-x}–0.3; (d) TiO_{2-x}–0.6; (e) TiO_{2-x}–0.9; (f) SEM images of TiO_{2-x}–0.9.

UV–vis DRS tests were performed on the prepared materials, the test results are shown in Figure 7(a). Compared with the TiO_{2-x} without HF added in the preparation process, the solar light absorption properties of the samples with HF added during the preparation were enhanced. The forbidden band width of each sample calculated by K–M function and Tauc equation is shown in Figure 7(b). The bandgap of TiO_2 decreases gradually with the increase of the amount of HF added. When the amount of HF added is 0.9 mL, the bandgap of TiO_{2-x}–0.9 is 2.76 eV. It is generally believed that the fluorine atom itself cannot reduce the bandgap width, but the fluorine element can stabilize the surface Ti^{3+} and oxygen vacancies and promote their formation [35, 43]. Therefore, the fluorination treatment can affect the energy band structure of the material and improves the absorption range of sunlight. Although TiO_{2-x}–0.9 has the largest light absorption range, TiO_{2-x}–0.3 has the best photocatalytic performance in the photocatalytic degradation test. Based on the results of XRD and TEM analyses, with the increase of HF addition, the grain size of TiO_2 gradually became larger, resulting in a decrease in specific surface area, which, in turn, reduced the photocatalytic performance.

In order to further investigate the applicability of F-TiO_{2-x} photocatalyst, TiO_{2-x}–0.3 with the best photocatalytic performance was selected as the photocatalyst to investigate its degradation of different reaction substrates. In the experiment, the same concentrations of MO and MB were selected for comparison with the RhB used in the previous experiments. The obtained experimental results are shown in Figure 8. The results show that TiO_{2-x}–0.3

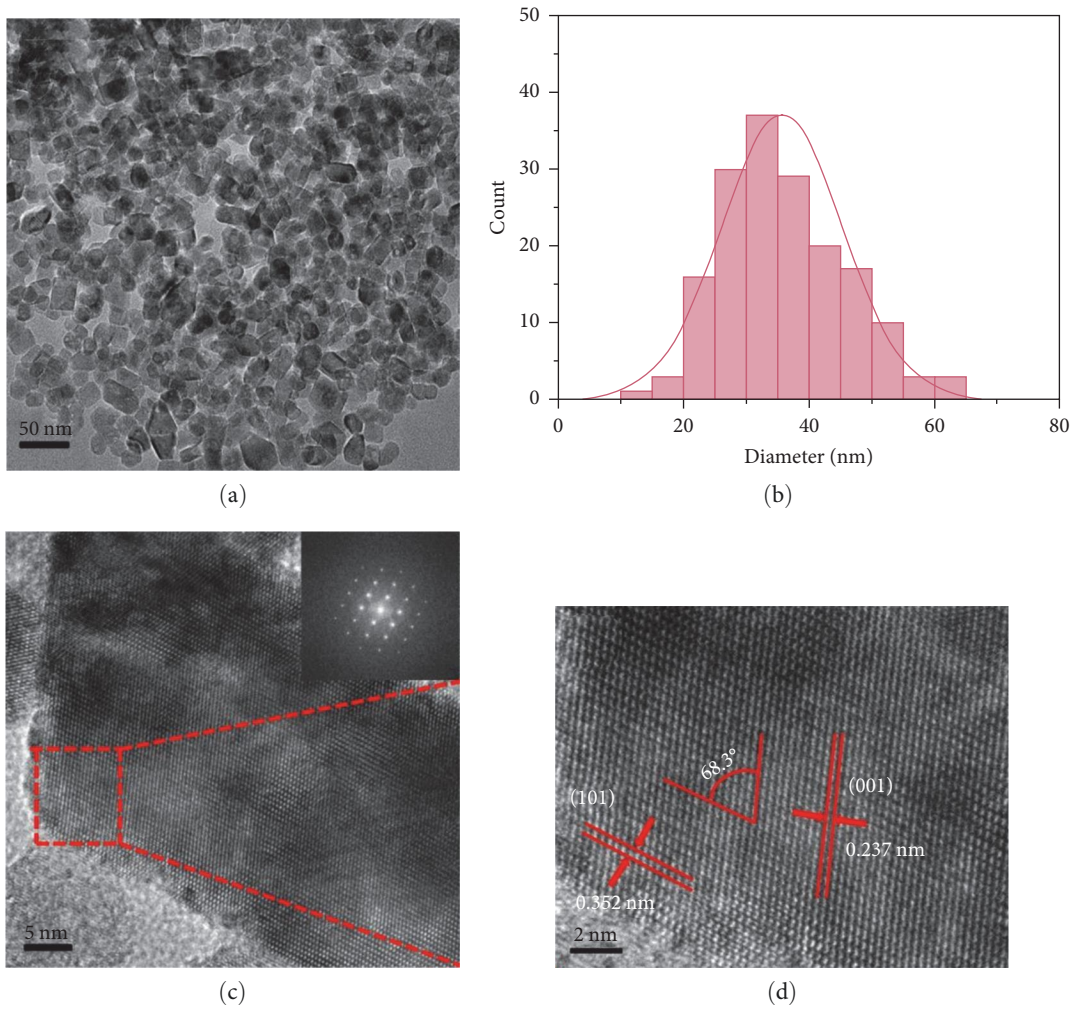

Figure 5: (a) TEM image of TiO_{2-x}–0.3; (b) particle size distribution image; (c) HRTEM image; (d) HRTEM enlarged image.

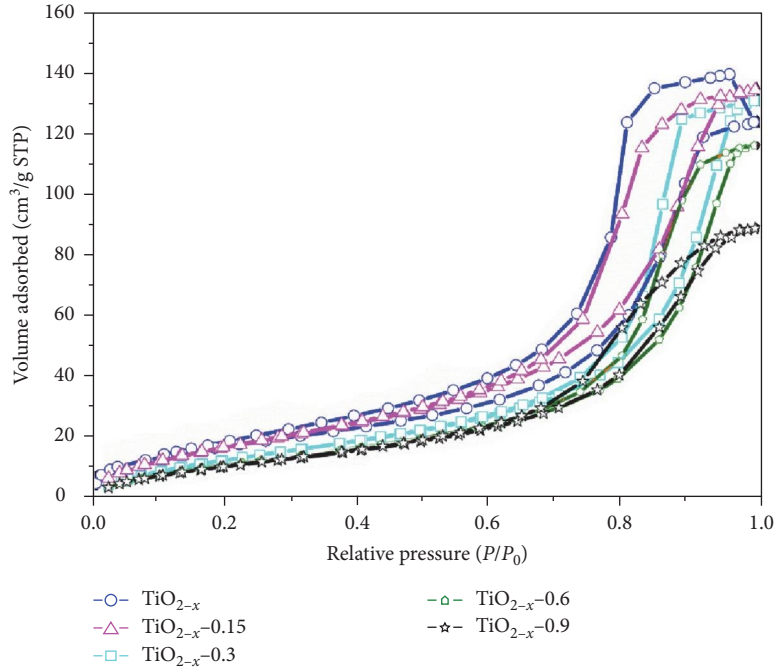

Figure 6: Nitrogen adsorption/desorption isotherms of F-TiO_{2-x} prepared with different HF usage.

Table 3: The specific surface area of F-TiO_{2-x} prepared with different amounts of HF.

Samples	TiO_{2-x}	TiO_{2-x}–0.15	TiO_{2-x}–0.3	TiO_{2-x}–0.6	TiO_{2-x}–0.9
Specific surface area (m^2/g)	81.2	71.5	60.1	49.3	28.5

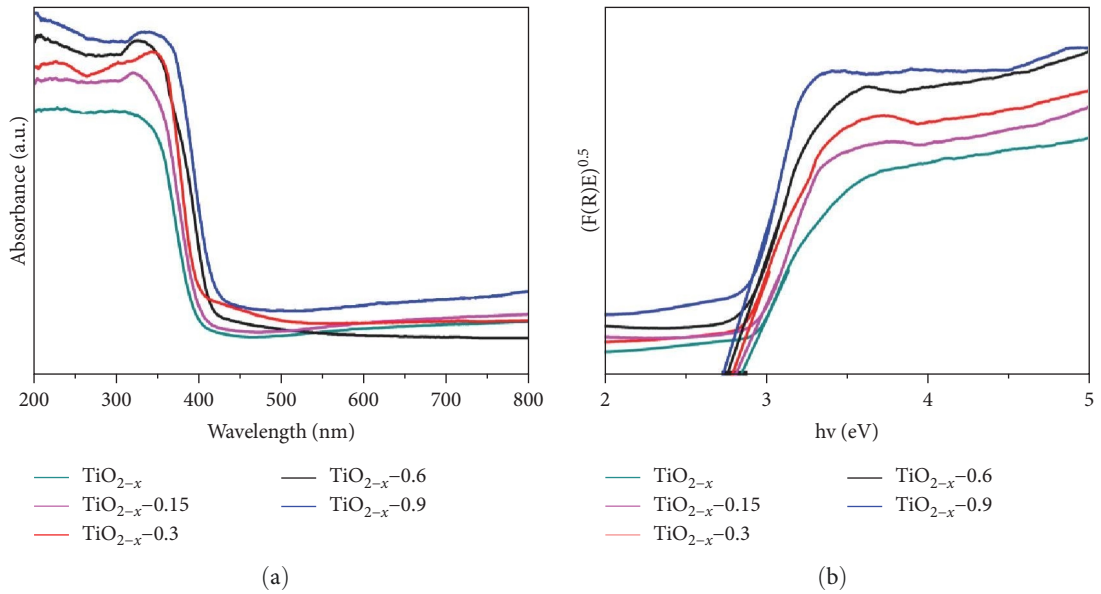

Figure 7: (a) DRS diagrams of F-TiO_{2-x} catalysts prepared with different HF usage; (b) calculation and analysis diagram of forbidden band width.

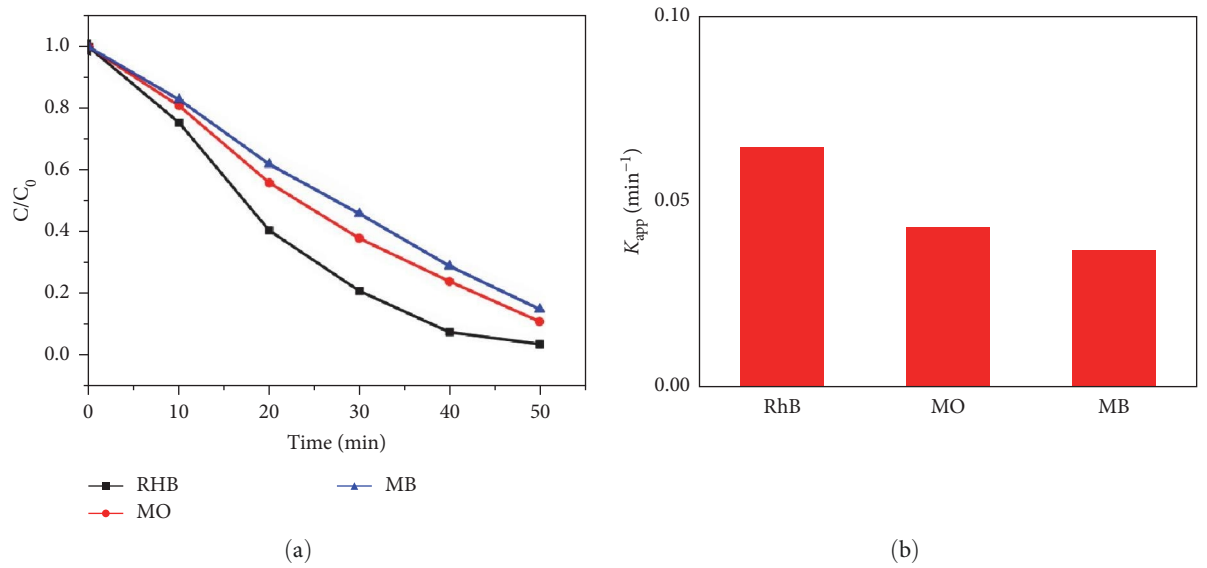

Figure 8: (a) Comparison of degradation performance of TiO_{2-x}–0.3 for different substrates; (b) first-order kinetic constant diagram.

has different photocatalytic degradation performance for different reaction substrates and also the best degradation performance for RhB, with a degradation rate of 96.8%, followed by MO with a degradation rate of 89%, and the worst with MB with a degradation rate of 85%. Figure 8(b) shows the kinetic constants of TiO_{2-x}–0.3 for different reaction substrates. From the kinetic constants, it can be inferred that the degradation rates of different substrates are RhB > MO > MB in order from fast to slow. This shows that the degradation performance of TiO_{2-x}–0.3 for different reaction substrates is still very different. As shown in Table 4, compared with TiO_{2-x}, the photocatalytic performance of F-TiO_{2-x} is improved [44].

We also investigate the stability of F-TiO_{2-x} photocatalyst, TiO_{2-x}–0.3 with the best photocatalytic performance was selected as the photocatalyst and RhB as the degradation

Table 4: Comparison of photocatalytic performance of TiO_{2-x} and F-TiO_{2-x}.

		RhB	MO	MB
TiO_{2-x}	Kinetic constant (min^{-1})	0.0518	0.0383	0.0321
	Degradation rate (%)	94.8	90.3	83.9
F-TiO_{2-x}	Kinetic constant (min^{-1})	0.0658	0.0421	0.0397
	Degradation rate (%)	96.8	89	85

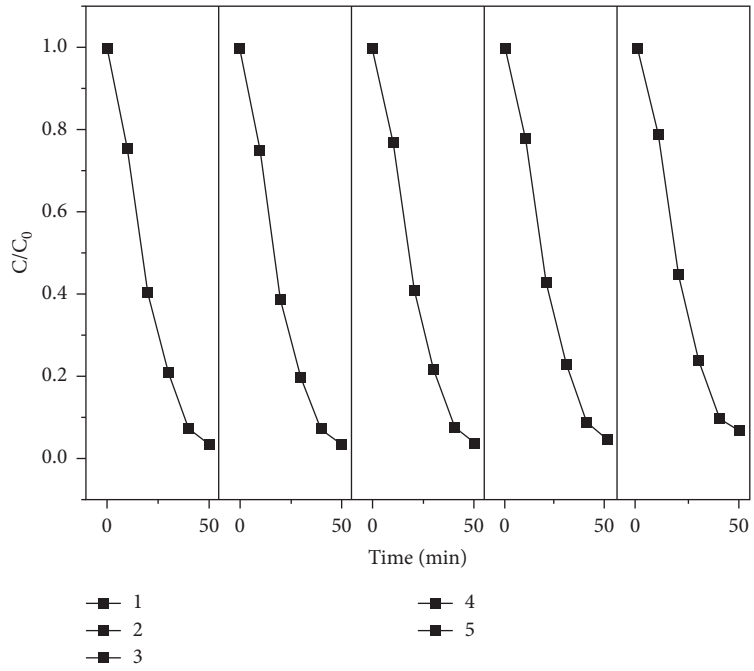

Figure 9: Recycling degradation performance of TiO_{2-x}–0.3.

substrate. The test method of the cycle stability of the experiment in this chapter is the same as that of the previous chapter, and the experiment tests the cycle performance of the material. After the first degradation process, the photocatalytic reaction material was obtained by centrifugation and directly freeze-dried without cleaning. After the material was dried, the next photocatalytic degradation experiment was performed, which was repeated five times. The experimental results are shown in Figure 9. The experimental results show that the initial degradation rate of TiO_{2-x}–0.3 photocatalyst is 96.8%, and after five cycles of use, the degradation rate still reaches 95%, and TiO_{2-x}–0.3 still maintains a blue appearance. The stability test of the sample TiO_{2-x} shows that with the increase in the number of cycles, the photocatalytic degradation performance decreases, and the sample gradually turns white after being exposed to the air for a period of time. For samples treated with HF, the blue color remained stable. The comparison shows that the stability of TiO_{2-x}–0.3 is greatly improved compared with that of TiO_{2-x}. This indicates that the surface fluorination treatment is beneficial to the formation and stable existence of Ti^{3+} and oxygen vacancies on the surface of TiO_{2-x} [35, 45].

Understanding the active species during the degradation of RhB by F-TiO_{2-x} is essential for analyzing the photocatalytic reaction mechanism. In order to explore the active species in the process of F-TiO_{2-x} degradation of RhB, the corresponding active species of different radical scavengers were added, and then the changes of the degradation effects were compared to obtain the role of different active species in the reaction process. The transfer of electrons and holes is very important in the photocatalytic process. The catalytic ability of a catalyst depends on the electron–hole pair, the separation of photogenerated electrons and holes is considered to be the initial step in the photocatalytic degradation process. For these reasons, electrons and holes were first trapped, holes (h^+) were removed by ammonium oxalate, and electrons were captured by $AgNO_3$. As shown in Figure 10, it is the effect of adding different radical scavengers on the degradation of RhB by F-TiO_{2-x}. When ammonium oxalate was added, the degradation rate became 70% of the original, and after adding $AgNO_3$, the degradation rate became 58% of the original. Tests show that electrons and holes play an important role in the photocatalytic degradation process. The photogenerated holes react with OH^- or H_2O adsorbed on the surface to generate hydroxyl radicals (·OH), and the photogenerated electrons can react with O_2 to generate superoxide radicals ($\cdot O_2^-$). In this experiment, isopropanol was used to remove hydroxyl radicals (·OH). After adding isopropanol, the degradation rate of RhB became 86% of the original. The superoxide radical ($\cdot O_2^-$) was removed by *p*-benzoquinone, and the degradation

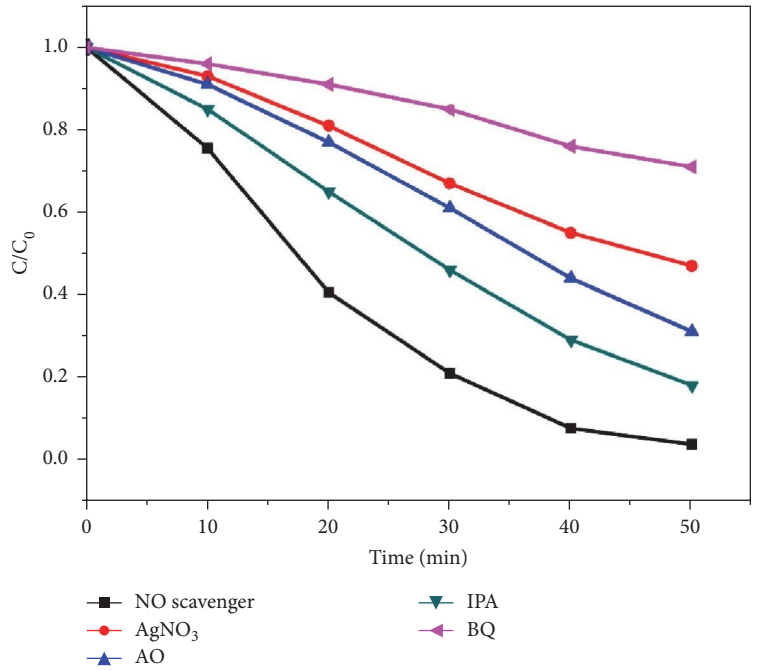

Figure 10: Effect of active species scavenger on the degradation performance of TiO_{2-x}–0.3.

rate of RhB after the addition of *p*-benzoquinone became 30% of the original. Photogenerated electrons have excellent reducibility and cannot oxidize organic pollutants themselves, but the test results show that photogenerated electrons have a great influence on the photocatalytic degradation rate. This is because photogenerated electrons affect the formation of superoxide radicals ($\cdot O_2^-$), whereas photogenerated holes have a greater effect on the photocatalytic degradation rate than hydroxyl radicals (·OH), indicating that photogenerated holes not only affect hydroxyl radicals (·OH) but also oxidize organic pollutants by itself. By analyzing the effect of different active species scavengers on the photocatalytic reaction, it is seen that superoxide radical ($\cdot O_2^-$) is the main active species in the process of photocatalytic degradation of RhB, and photogenerated holes can also directly oxidize organic pollutants, and photogenerated electrons affect the formation of superoxide radicals ($\cdot O_2^-$).

Based on the above information, the band structure diagram and possible charge separation process of TiO_{2-x}–0.3 are shown in Figure 11. New secondary states appear near the conduction band (CB) edge of TiO_2 due to Ti^{3+} doping or oxygen vacancies, and the doped N atoms generate new impurity levels above the valence band (VB) of TiO_2. Narrowing the bandgap of TiO_2 can enhance the visible light absorption. Under visible light irradiation, electrons in the CB of anatase, TiO_2 are transferred to the CB of TiO_2. Electrons in the CB can react with dissolved oxygen and generate superoxide radicals ($\cdot O_2^-$), and holes in the VB can oxidize surface OH^- or adsorb water to generate hydroxyl radicals (·OH), which can also RhB adsorbed on the oxidized surface. ·OH, $\cdot O_2^-$, and h^+ of highly active substances have strong oxidative ability for the degradation of organic pollutants.

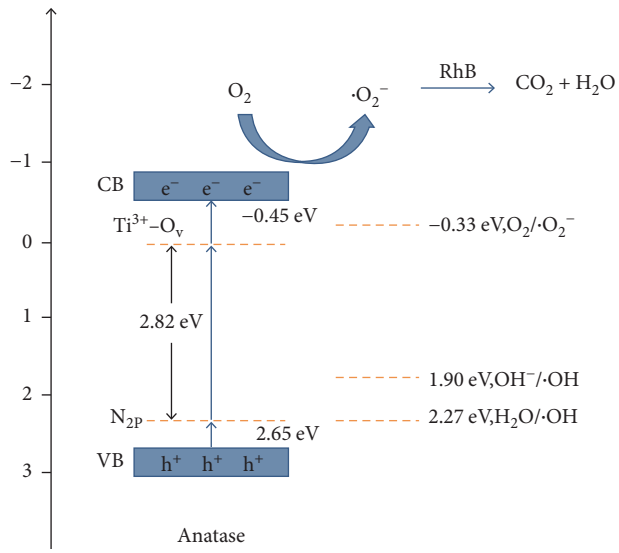

Figure 11: Photocatalytic degradation mechanism of rhodamine B by F-TiO_{2-x}.

4. Conclusions

In this paper, F-TiO_{2-x} photocatalytic material was prepared by hydrothermal method. We have investigated the effect of the degree of fluorination on the photocatalytic properties of the material, and the recycling stability and applicability of the prepared materials under the optimal degree of fluorination. We also explored the types of active species in the process of photocatalytic degradation of materials, and studied the mechanism of photocatalytic degradation of RhB. The results showed that the fluorine element etched the

edge part of TiO_{2-x}, which promoted the self-assembly of small TiO_{2-x} particles and gradually formed large particles. At the same time, fluorine element can be effective for stabilizing Ti^{3+} and oxygen vacancies on the surface of TiO_{2-x}. With the increase in the amount of HF added, the photocatalytic performance of the prepared material is first increased and then decreased. The high-energy surface (001) was successfully exposed when the material prepared with the addition of 0.3 mL of HF. The F-TiO_{2-x} catalysts still showed great differences in the degradation performance of different organic dyes. Among them, the degradation effect of RhB is the best, followed by MO and MB, which indicates that the catalyst has a relatively wide range of applications.

Data Availability

The data used to support the findings of this study are available from the corresponding author upon request.

Acknowledgments

This work has been financially supported by the National Natural Science Foundation of China (grant numbers 51904128, 51902145), the Doctoral Start-up Fund Research supported by Jinling Institute of Technology (grant numbers jit-b-202026, jit-b-201905), the research grants from Six Talent Peaks Project in Jiangsu Province (grant number XCL-109), and the training objects of young academic leaders of Cyan Engineering in Jiangsu Province.

Conflicts of Interest

The authors declare that they have no conflicts of interest.

References

[1] A. S. M. Nur, M. Sultana, A. Mondal et al., "A review on the development of elemental and codoped TiO_2 photocatalysts for enhanced dye degradation under UV–vis irradiation," *Journal of Water Process Engineering*, vol. 47, Article ID 102728, 2022.

[2] C. Yu, M. Tan, C. Tao et al., "Remarkably enhanced piezo-photocatalytic performance in $BaTiO_3$/CuO heterostructures for organic pollutant degradation," *Journal of Advanced Ceramics*, vol. 11, pp. 414–426, 2022.

[3] J. Wu, L. Li, X.-a. Li, X. Min, and Y. Xing, "A novel 2D graphene oxide modified α-$AgVO_3$ nanorods: design, fabrication, and enhanced visible-light photocatalytic performance," *Journal of Advanced Ceramics*, vol. 11, pp. 308–320, 2022.

[4] C. A. Bode-Aluko, O. Pereao, H. H. Kyaw et al., "Photocatalytic and antifouling properties of electrospun TiO_2 polyacrylonitrile composite nanofibers under visible light," *Materials Science and Engineering: B*, vol. 264, Article ID 114913, 2021.

[5] A. ul Ahmad, A. Abbas, S. Ali et al., "Visible-light driven photo-catalytic performance of novel composite of TiO_2 and fluorinated hexagonal boron nitride nanosheets," *Ceramics International*, vol. 47, no. 7, Part A, pp. 10089–10095, 2021.

[6] K. Nakata and A. Fujishima, "TiO_2 photocatalysis: design and applications," *Journal of Photochemistry and Photobiology C: Photochemistry Reviews*, vol. 13, no. 3, pp. 169–189, 2012.

[7] K. Kannan, D. Radhika, R. D. Kasai et al., "Facile fabrication of novel ceria-based nanocomposite (CYO-CSO) via co-precipitation: electrochemical, photocatalytic and antibacterial performances," *Journal of Molecular Structure*, vol. 1256, Article ID 132519, 2022.

[8] N. Suganthi, S. Thangavel, and K. Kannan, "*Hibiscus subdariffa* leaf extract mediated 2-D fern-like ZnO/TiO_2 hierarchical nanoleaf for photocatalytic degradation," *FlatChem*, vol. 24, Article ID 100197, 2020.

[9] K. Kannan, D. Radhika, A. S. Nesaraj, K. K. Sadasivuni, and L. Sivarama Krishna, "Facile synthesis of NiO-CYSO nanocomposite for photocatalytic and antibacterial applications," *Inorganic Chemistry Communications*, vol. 122, Article ID 108307, 2020.

[10] A. Sathiya Priya, D. Geetha, K. Karthik, and M. Rajamoorthy, "Investigations on the enhanced photocatalytic activity of (Ag, La) substituted nickel cobaltite spinels," *Solid State Sciences*, vol. 98, Article ID 105992, 2019.

[11] M. Ge, Z. Hu, J. Wei, Q. He, and Z. He, "Recent advances in persulfate-assisted TiO_2-based photocatalysis for wastewater treatment: performances, mechanism and perspectives," *Journal of Alloys and Compounds*, vol. 888, Article ID 161625, 2021.

[12] R. Taziwa, E. L. Meyer, E. Sideras-Haddad, R. M. Erasmus, E. Manikandan, and B. W. Mwakikunga, "Effect of carbon modification on the electrical, structural, and optical properties of TiO_2 electrodes and their performance in labscale dye-sensitized solar cells," *International Journal of Photoenergy*, vol. 2012, Article ID 904323, 9 pages, 2012.

[13] S. S. Amin, S.-Y. Li, X. Wu, W. Ding, and T. T. Xu, "Facile synthesis and tensile behavior of TiO_2 one-dimensional nanostructures," *Nanoscale Research Letters*, vol. 5, no. 2, pp. 338–343, 2009.

[14] Y. Ge, H. Luo, J. Huang, and Z. Zhang, "Visible-light-active TiO_2 photocatalyst for efficient photodegradation of organic dyes," *Optical Materials*, vol. 115, Article ID 111058, 2021.

[15] Q. Guo, C. Zhou, Z. Ma, and X. Yang, "Fundamentals of TiO_2 photocatalysis: concepts, mechanisms, and challenges," *Advanced Materials*, vol. 31, no. 50, Article ID e1901997, 2019.

[16] R. Katal, S. Masudy-Panah, M. Tanhaei, M. H. D. A. Farahani, and H. Jiangyong, "A review on the synthesis of the various types of anatase TiO_2 facets and their applications for photocatalysis," *Chemical Engineering Journal*, vol. 384, Article ID 123384, 2020.

[17] Z. Zhou, Y. Yu, Z. Ding, M. Zuo, and C. Jing, "Modulating high-index facets on anatase TiO_2," *European Journal of Inorganic Chemistry*, vol. 2018, pp. 683–693, 2018.

[18] Y. Liang, Y. Yang, H. Zhou et al., "A systematic study on the crystal facets-dependent gas sensing properties of anatase TiO_2 with designed {010}, {101} and {001} facets," *Ceramics International*, vol. 45, no. 5, pp. 6282–6290, 2019.

[19] Z. P. Tshabalala, T. P. Mokoena, K. T. Hillie, H. C. Swart, and D. E. Motaung, "Improved BTEX gas sensing characteristics of thermally treated TiO_2 hierarchical spheres manifested by high-energy {001} crystal facets," *Sensors and Actuators B: Chemical*, vol. 338, Article ID 129774, 2021.

[20] M. Motola, M. Čaplovičová, M. Krbal et al., "Ti^{3+} doped anodic single-wall TiO_2 nanotubes as highly efficient photocatalyst," *Electrochimica Acta*, vol. 331, Article ID 135374, 2020.

[21] L. Li, X. Chen, Z. Liu, X. Quan, F. Qiu, and X. Zhang, "Synthesis of CuO*x*/TiO_2 photocatalysts with enhanced photocatalytic performance," *SSRN Electronic Journal,* 2022.

[22] X.-j. Wang, W.-y. Yang, F.-t. Li, Y.-b. Xue, R.-h. Liu, and Y.-j. Hao, "In situ microwave-assisted synthesis of porous N-TiO_2/g-C_3N_4 heterojunctions with enhanced visible-light photocatalytic properties," *Industrial and Engineering Chemistry Research*, vol. 52, no. 48, pp. 17140–17150, 2013.

[23] M. Zulfiqar, S. Sufian, A. Bahadar, N. Lashari, N. E. Rabat, and N. Mansor, "Surface-fluorination of TiO_2 photocatalysts for remediation of water pollution: a review," *Journal of Cleaner Production*, vol. 317, Article ID 128354, 2021.

[24] J. Gou, Q. Ma, X. Deng et al., "Fabrication of Ag_2O/TiO_2-Zeolite composite and its enhanced solar light photocatalytic performance and mechanism for degradation of norfloxacin," *Chemical Engineering Journal*, vol. 308, pp. 818–826, 2017.

[25] M. Humayun, A. Zada, Z. Li et al., "Enhanced visible-light activities of porous $BiFeO_3$ by coupling with nanocrystalline TiO_2 and mechanism," *Applied Catalysis B: Environmental*, vol. 180, pp. 219–226, 2016.

[26] M. Du, B. Qiu, Q. Zhu, M. Xing, and J. Zhang, "Fluorine doped TiO_2/mesocellular foams with an efficient photocatalytic activity," *Catalysis Today*, vol. 327, pp. 340–346, 2019.

[27] A. El Gaidoumi, A. Loqman, M. Zouheir et al., "Sol–gel fluorinated TiO_2-clay nanocomposite: study of fluor-titanium interaction on the photodegradation of phenol," *Research on Chemical Intermediates*, vol. 47, pp. 5203–5228, 2021.

[28] J. C. Yu, J. Yu, W. Ho, Z. Jiang, and L. Zhang, "Effects of F^- doping on the photocatalytic activity and microstructures of nanocrystalline TiO_2 powders," *Chemistry of Materials*, vol. 14, no. 9, pp. 3808–3816, 2002.

[29] H. Park and W. Choi, "Effects of TiO_2 surface fluorination on photocatalytic reactions and photoelectrochemical behaviors," *The Journal of Physical Chemistry B*, vol. 108, pp. 4086–4093, 2004.

[30] Y. Zhang, M. Wu, Y. Wang et al., "Fluorinated TiO_2 coupling with α-MnO_2 nanowires supported on different substrates for photocatalytic VOCs abatement under vacuum ultraviolet irradiation," *Applied Catalysis B: Environmental*, vol. 280, Article ID 119388, 2021.

[31] Z. Liu, M. Yu, X. Wang et al., "Sandwich shelled TiO_2@-Co_3O_4@Co_3O_4/C hollow spheres as anode materials for lithium ion batteries," *Chemical Communications (Cambridge, England)*, vol. 57, no. 14, pp. 1786–1789, 2021.

[32] P. Zheng, T. Liu, Y. Su, L. Zhang, and S. Guo, "TiO_2 nanotubes wrapped with reduced graphene oxide as a high-performance anode material for lithium-ion batteries," *Scientific Report*, vol. 6, Article ID 36580, 2016.

[33] P. Zheng, H. Wu, J. Guo, J. Dong, S. Jia, and Z. Zhu, "P-N co-doping induced structural recovery of TiO_2 for overall water splitting under visible light irradiation," *Journal of Alloys and Compounds*, vol. 615, pp. 79–83, 2014.

[34] R. Hong, J. Shi, Z. Li et al., "Surface enhanced Raman scattering of defective TiO_2 thin film decorated with silver nanoparticles by laser ablation," *Optical Materials*, vol. 109, Article ID 110338, 2020.

[35] Y. Wang, Y. Zhang, X. zhu, Y. Liu, and Z. Wu, "Fluorine-induced oxygen vacancies on TiO_2 nanosheets for photocatalytic indoor VOCs degradation," *Applied Catalysis B: Environmental*, vol. 316, Article ID 121610, 2022.

[36] N. Roy, Y. Park, Y. Sohn, K. T. Leung, and D. Pradhan, "Green synthesis of anatase TiO_2 nanocrystals with diverse shapes and their exposed facets-dependent photoredox activity," *ACS Applied Materials and Interfacess*, vol. 6, no. 19, pp. 16498–16507, 2014.

[37] N. Fessi, M. F. Nsib, L. Cardenas et al., "Surface and electronic features of fluorinated TiO_2 and their influence on the photocatalytic degradation of 1-methylnaphthalene," *The Journal of Physical Chemistry C*, vol. 124, no. 21, pp. 11456–11468, 2020.

[38] B. Wu, Y. Sun, J. Dong, Z. Tian, Y. Xie, and J. Hou, "Nitrogen and fluorine codoped TiO_2 nanotube arrays: operation sequence of solvothermal/annealing treatment and photocatalytic performance," *Journal of Alloys and Compounds*, vol. 898, Article ID 162770, 2022.

[39] Q. Wang, B. Rhimi, H. Wang, and C. Wang, "Efficient photocatalytic degradation of gaseous toluene over F-doped TiO_2/exfoliated bentonite," *Applied Surface Science*, vol. 530, Article ID 147286, 2020.

[40] Q. Gao, F. Si, S. Zhang, Y. Fang, X. Chen, and S. Yang, "Hydrogenated F-doped TiO_2 for photocatalytic hydrogen evolution and pollutant degradation," *International Journal of Hydrogen Energy*, vol. 44, no. 16, pp. 8011–8019, 2019.

[41] L. Yang, Q. Zhang, W. Wang et al., "Tuning the photoelectronic and photocatalytic properties of single-crystalline TiO_2 nanosheet array films with dominant {001} facets by controlling the hydrochloric acid concentration," *Journal of Materials Science*, vol. 51, pp. 950–957, 2015.

[42] Y.-E. Du, X. Niu, X. He, K. Hou, H. Liu, and C. Zhang, "Synthesis and photocatalytic activity of TiO_2/CdS nanocomposites with co-exposed anatase highly reactive facets," *Molecules (Basel, Switzerland)*, vol. 26, no. 19, Article ID 6031, 2021.

[43] R. Xie, D. Lei, Y. Zhan et al., "Efficient photocatalytic oxidation of gaseous toluene over F-doped TiO_2 in a wet scrubbing process," *Chemical Engineering Journal*, vol. 386, Article ID 121025, 2020.

[44] Y. Zhao, M. Zhang, W. Wang, W. Song, K. Jiang, and X. Zhang, "Preparation of Ti^{3+}/N-co-doped TiO_2 by one-step hydrothermal synthesis method with high photocatalytic degradation performance under visible light," *Journal of Materials Science: Materials in Electronics*, vol. 32, pp. 22910–22920, 2021.

[45] F. Pellegrino, E. Morra, L. Mino, G. Martra, M. Chiesa, and V. Maurino, "Surface and bulk distribution of fluorides and Ti^{3+} species in TiO_2 nanosheets: implications on charge carrier dynamics and photocatalysis," *The Journal of Physical Chemistry C*, vol. 124, no. 5, pp. 3141–3149, 2020.